Rate Constants, $1100 \leq T \leq 2000$ K, for $H + NO_2 \rightarrow OH + NO$ Using Two Shock Tube Techniques: Comparison of Theory to Experiment†

M.-C. Su,‡ S. S. Kumaran, K. P. Lim, J. V. Michael,* A. F. Wagner,* L. B. Harding,* and D.-C. Fang

Chemistry Division, Argonne National Laboratory, Argonne, Illinois 60439

Received: November 8, 2001; In Final Form: January 7, 2002

Rate constants for the reaction $H + NO_2 \rightarrow OH + NO$ have been measured over the temperature range 1100−2000 K in reflected shock wave experiments using two different methods of analysis. In both methods, the source of H-atoms is from ethyl radical decomposition in which the radicals are formed essentially instantaneously from the thermal decomposition of C_2H_5I. The first method uses atomic resonance absorption spectrometry (ARAS) to follow the temporal behavior of H-atoms. Experiments were performed under such low $[C_2H_5I]_0$ that the title reaction could be chemically isolated, and the decay of H-atoms was strictly first-order. The results from these experiments can be summarized as $k = (1.4 \pm 0.3) \times 10^{-10}$ cm^3 molecule^{-1} s^{-1} for $1100 \leq T \leq 1650$ K. The second method utilizes a multipass optical system for observing the product radical, OH. A resonance lamp was used as the absorption source. Because this is the first OH-radical kinetics investigation from this laboratory, extensive calibration was required. This procedure resulted in a modified Beer's law description of the curve-of-growth, which could subsequently be used to convert absorption data to OH-radical profiles. Rate constants by this method required chemical simulation, and the final result can be summarized as $k = (1.8 \pm 0.2) \times 10^{-10}$ cm^3 molecule^{-1} s^{-1} for $1250 \leq T \leq 2000$ K. Because the results from the two methods statistically overlap, they can be combined giving $k = (1.64 \pm 0.30) \times 10^{-10}$ cm^3 molecule^{-1} s^{-1} for $1100 \leq T \leq 2000$ K. The present results are compared to earlier work at lower temperatures, and the combined database yields the temperature dependence over the large range, 195−2000 K. The combined results can be summarized as $k = (1.47 \pm 0.26) \times 10^{-10}$ cm^3 molecule^{-1} s^{-1} for $195 \leq T \leq 2000$ K. The reaction is subsequently considered theoretically using ab initio electronic structure calculations combined with modern dynamical theory to rationalize the thermal rate behavior.

Introduction

The reaction

$$H + NO_2 \rightarrow OH + NO \qquad (1)$$

has been of interest in chemical kinetics and dynamics for over 35 years.[1−9] The reaction has been used for a variety of purposes, and this has fostered the continuing interest. In discharge flow tube investigations, it has been used as a source for both ground-state and vibrationally excited OH-radicals for the study of the reactions of these species with molecules.[10,11] It has been used as a calibration reaction for determining absolute H-atom concentrations in discharge flow tube studies.[12,13] It is an interesting reaction because the OH that is produced has a nonthermal vibrational distribution; that is, it is vibrationally hot.[14−19] The lowest energy dynamical experiments at a relative collision energy of 0.93 kcal mol^{-1} document forward peaking in the product angular distribution suggesting an adduct lifetime that is less than a rotational period.[18] Hence, questions concerning the randomization of energy have to be considered in the theoretical interpretation of results on this reaction. Last, the reaction is now known to be important in the high-temperature combustion kinetics of nitramine propellants.[20]

The most recent thermal rate constant investigations all agree within experimental error that $k_1 \cong 1.3 \times 10^{-10}$ cm^3 molecule^{-1} s^{-1} at room temperature.[4−9] If the results prior to 1979 are excluded, there is also a consensus that there is little or no temperature dependence up to 760 K. The temperature invariance led Michael et al.[7] to suggest that the rate constant was determined solely by the collision rate and that there was no electronic energy barrier for the reaction. Ko and Fontijn[9] agree with this latter point as do the dynamical studies even though there is some question as to the extent of energy randomization in the vibrationally excited adduct.[15,16,18] Ko and Fontijn[9] also discuss the possibility of collisional stabilization with the detailed mechanism $H + NO_2 \rightleftharpoons HONO^* \rightarrow OH + NO$ followed by $HONO^* + M \rightarrow HONO + M$. Of course, the question of stabilization is irrelevant at usual pressures if the reaction is direct; that is, the lifetime of the adduct is the same magnitude as that for a vibration. Irrespective of the adduct lifetime, the dissociation channel is exothermic relative to reactants by 29.6 kcal mol^{-1} at 0 K; that is, the dissociation channel is lower-lying than the reactants. Because there is no electronic barrier for association, the rate of reaction will depend on long-range forces and the effective transition state (or states) will be loose and near to reactants. The reaction then represents a classic atom−radical recombination with a low-lying dissociation channel, and the rate constant will be equal to that for the infinite pressure limit. Hence, the reaction then becomes quite interesting from a theoretical point of view.

† Part of the special issue "Donald Setser Festschrift".

* To whom correspondence should be addressed.

‡ Sabbatical Leave. Permanent address: Department of Chemistry, Butler University, Indianapolis, IN 46208.

10.1021/jp0141023 CCC: $22.00
Published on Web 03/06/2002

In this paper, the rate constants are measured in reflected shock waves using two different observations, H-atom depletion and OH-radical formation. Experiments have been performed from 1100 to 2000 K. These data are combined with the lower temperature sets giving a composite rate behavior over the large temperature range, 195−2000 K. New ab initio potential energy calculations are also presented, and dynamics calculations based on the theoretical potential energy surface are also presented and compared to experiment.

Experimental Section

Most of the experimental methods and techniques are described elsewhere;[21,22] however, in the present study, some substantial modifications to the apparatus have been made in preparation for multipass optical absorption experiments in the reflected shock wave regime.[23]

Apparatus. The present experiments were performed in a redesigned apparatus. The shock tube is constructed from 304 stainless steel in three sections. The first 4 in. o.d. cylindrical section is separated from the He driver chamber by a 4 mil unscored 1100-H18 aluminum diaphragm. A 0.25 m transition section then connects the first and third sections. The third section is of rounded-corner (radius, 1.71 cm) square design and is fabricated from flat stock (3 mm) with a mirror finish. Two sets of flat MgF_2 crystal windows (2.54 cm) are mounted with high-vacuum epoxy cement normal to one another at a distance of 6 cm from the endplate. The aperture diameter is 2.29 cm. One set is used for atomic resonance absorption spectrometric (ARAS) detection of H-atoms, and the other set is used for OH-radical absorption using a multipass optical technique. The windows are flush to the polished inside wall of the tube. The path length between windows is 8.745 cm. All connections are made through Varian "Conflat" flanges with copper gaskets. As before,[21,22] the incident shock wave velocities are measured with eight fast pressure transducers (PCB Piezotronics, Inc., model 113A21), and both the velocity and absorption signals are recorded with a digital oscilloscope (Nicolet, model 4094C). The shock tube was routinely pumped between experiments to $<10^{-8}$ Torr by an Edwards Vacuum Products model CR100P packaged pumping system. Temperature and density in the reflected shock wave regime were calculated from measured incident shock wave velocity and initial thermodynamic conditions. This procedure has been given previously, and corrections for boundary layer perturbations have been applied.[24−26]

H-Atom ARAS Detection. The ARAS technique and photometer configuration for the detection of H-atoms has already been discussed in detail.[13,21,22] Unreversed H-atom Lyman-α ($Ly_{\alpha H}$) was produced by a 2450 MHz microwave discharge in a 1.7 Torr flow of prepurified He. This transition at 121.6 nm was further spectrally isolated by placing a 3 cm gas filter section that contains dry air at atmospheric pressure in front of the solar blind photomultiplier. There was always some radiation that is not $Ly_{\alpha H}$, and it was necessary to determine the fraction of this spectral impurity. Therefore, an H-atom filter section was placed in front of the resonance lamp.[27] This filter section is a fast discharge-flow system operating with ∼0.2 Torr of H_2. With the microwave discharge operating, sufficient H-atom concentration was produced in the optical path to nearly remove all $Ly_{\alpha H}$ radiation. The measurement of the fraction of light that was resonance radiation was routinely made before each kinetics experiment and allowed for the calculation of $(ABS)_H \equiv -\ln(I/I_0)$. In all experiments, $[H]_0$ was kept low so that Beer's law holds.[13] Hence, $(ABS)_H$ is directly proportional to [H] over the entire time span of a given experiment.

Detection by Multipass Optical Absorption. In this work, a long absorption path multipass detector system,[23] which is based on the original design of White[28] with modifications from Bernstein and Herzberg,[29] has been used. The optical configuration consists of an OH resonance lamp, three multipass reflectors (one split in half), an interference filter, and a photomultiplier tube. The OH absorption lamp was constructed from a 6.4 mm o.d. Pyrex tube. High-purity Ar at atmospheric pressure was bubbled through distilled water in a glass trap, and the mixture was then introduced through a needle valve into the low-pressure (∼4 Torr) lamp. The microwave discharge was operated at 50 W, and the resultant OH resonance radiation was focused at the center of the shock tube, between the two windows, with a 2.54 cm diameter planoconvex lens mounted on the end of the lamp. The multipass optical system is constructed from three concave reflectors with identical radii of curvature. The reflectors and mounts were supplied by Infrared Analysis, Inc., and the radius of curvature and the aperture of the reflectors were customed designed for the present separation and aperture of the windows. The reflectors are MgF_2-coated for use in the far UV region. The three pieces involved in the reflector system are mounted outside the shock tube next to the windows with the center points of the windows and mirrors all in a coaxial position. The optical cavity thus formed is a conjugated focus system, which induces the light to travel back and forth between the reflectors in multiple passes. The relative positions of images on the reflectors are determined by set screw adjustments, allowing for changes in the number of passes for use in an experiment. We have used 12 passes giving a path length of 104.9 cm in this work. The light leaves the multipass cavity through an exit notch and is focused onto an interference filter (308 nm, fwhm of 17 nm, from Oriel Corp.). Signal detection is with an RCA 1P28 PMT. The signal-to-noise ratio is typically ∼80 for 12 passes, and this has given quite satisfactory sensitivity for probing the kinetics of hydroxyl radicals.

Gases. Kr (scientific grade, 99.999%), used as the diluent, and O_2 (scientific grade, 99.999%) and H_2 (scientific grade, 99.9999%), used in the experimental mixtures, were obtained from MG Industries and were used without further purification. He, used as received as the driver gas, was purified grade (99.995%) and was obtained from Airco Industrial Gases. C_2H_5I (99%) from Aldrich Chemical Co., Inc. and technical grade NO_2 from Matheson Gas Products were both further purified by bulb-to-bulb distillation with the middle thirds being retained. All gas mixtures were accurately measured with a Baratron capacitance manometer and were stored in an all-glass vacuum line.

Results

Kinetics results were obtained by observing both H-atom depletion and OH-radical buildup in two separate sets of experiments. Concurrent observations could not be carried out because the H-atom ARAS method is much more sensitive than OH-radical detection even with multipass enhancement. In preparation for the latter experiments, [OH] calibration experiments were necessary. The calibration is an extension of a method used earlier for H-atoms[30] involving the thermal decomposition of C_2H_5I to give $C_2H_4 + H + I$ in two steps. Subsequently, the H-atoms produced by this method can react with added NO_2 giving $OH + NO$, and this is the basis for two of the OH-radical calibration schemes. At higher [OH], the usual H_2/O_2 branching chain reaction is used, and the combination of the three types of experiments gives a curve of growth for OH.[23]

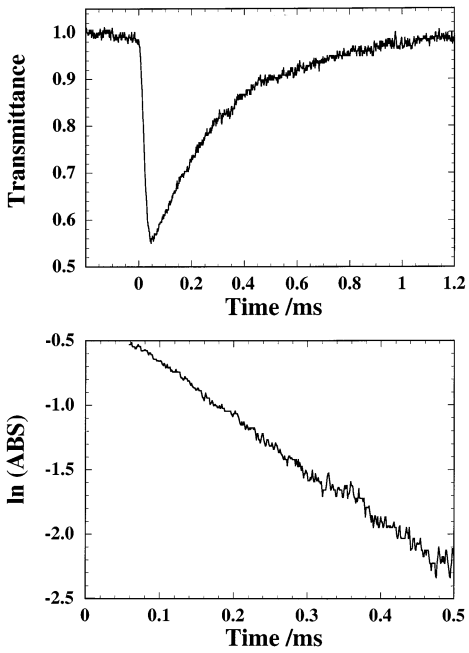

Figure 1. (top) A typical experimental record showing increasing H-atom ARAS signal due to reaction 1 after instantaneous [H] formation from C_2H_5I dissociation and (bottom) the first-order decay of atoms derived from the transmittance record (top) plotted as $\ln(ABS)_H$ against time. The negative slope, 3991 s^{-1}, is the first-order decay constant for $[C_2H_5I]_0 = 1.395 \times 10^{12}$ cm^{-3} and $[NO_2]_0 = 3.064 \times 10^{13}$ cm^{-3} giving $k_1 = 1.3 \times 10^{-10}$ cm^3 $molecule^{-1}$ s^{-1}. $T_5 = 1340$ K, $P_5 = 386$ Torr, and $\rho_5 = 2.780 \times 10^{18}$ cm^{-3}.

H-Atom Kinetics Analysis. Unlike previous studies from this laboratory in which H-atoms were produced by flash or laser photolysis,[21,22] here, the thermal decomposition of C_2H_5I supplies $[H]_0$ for the kinetics experiments. In earlier work, the thermal decomposition of C_2H_5I was studied, and by measuring yields of both [H] and [I] using ARAS techniques, it was shown that two decomposition pathways occur,[31]

$$C_2H_5I(+M) \rightarrow C_2H_5 + I(+M) \qquad (2a)$$

and

$$C_2H_5I(+M) \rightarrow C_2H_4 + HI(+M) \qquad (2b)$$

Following (2a), the ultrafast ethyl radical decomposition,

$$C_2H_5(+M) \rightarrow C_2H_4 + H(+M) \qquad (3)$$

gives H-atoms indicating that the overall process, eqs 2a and 3, is $C_2H_5I = C_2H_4 + H + I$. We found that $k_{2b} = 0.15k_{2a}$.[31] Above 1100 K, all processes are fast allowing for unambiguous kinetics experiments to be performed. As discussed earlier,[23] it can be shown with chemical simulations that the subsequent reactions of H- or I-atoms with either parent or product molecules are negligibly slow due to the very high sensitivity of the H-atom ARAS technique. Because H-atoms can be rapidly produced and observed at low concentrations by the C_2H_5I method, reaction 1 can be unambiguously studied provided the condition $[H]_0 \ll [NO_2]_0$ can be maintained. The top panel of Figure 1 shows a transmittance record from a typical experiment. Because $(ABS)_H$ is proportional to [H],[13] first-order decay constants can be determined from linear plots of $\ln(ABS)_H$ against time. This is illustrated in Figure 1 in which the plot determined from the top panel is shown in the bottom panel. The bimolecular rate constant for reaction 1 can then be determined by dividing the first-order decay constant by $[NO_2]_0$. Eighteen experiments between 1100 and 1650 K were carried out with a 22-fold excess of added NO_2. The conditions for these experiments and results for k_1 are given in Table 1. Even though the two lowest-pressure experiments give slightly higher results, there is no reason to reject these two experiments. Hence, there is then no obvious temperature dependence for the reaction over the temperature range of the experiments. The results can then be summarized by the expression

$$k_1 = (1.4 \pm 0.3) \times 10^{-10}\ cm^3\ molecule^{-1}\ s^{-1} \quad \text{for} \quad 1100 \le T \le 1650\ K \qquad (4)$$

where the error is one standard deviation.

TABLE 1: High-Temperature Rate Data for H + NO_2 Using H-atom Detection

$P_5{}^b$ (Torr)	$M_s{}^a$	$\rho_5{}^b$ (10^{18} cm^{-3})	$T_5{}^b$ (K)	k_{first} (s^{-1})	$k_1{}^c$ (10^{-10} cm^3 s^{-1})^c
$X_{C_2H_5I} = 5.018 \times 10^{-7}$, $X_{NO_2} = 1.102 \times 10^{-5}$					
386	2.290	2.780	1340	3991	1.3
428	2.377	2.897	1426	4670	1.5
548	2.608	3.140	1684	4368	1.3
507	2.534	3.064	1600	4443	1.3
424	2.370	2.877	1424	4070	1.3
344	2.203	2.661	1247	3388	1.2
119	2.169	0.948	1210	2394	2.3
163	2.394	1.089	1447	1855	1.6
167	2.430	1.084	1491	1645	1.4
173	2.446	1.108	1504	1717	1.4
136	2.250	1.019	1292	2296	2.0
151	2.341	1.051	1388	1841	1.6
266	2.295	1.916	1339	2388	1.1
366	2.569	2.146	1646	3213	1.4
354	2.537	2.124	1608	3140	1.3
270	2.304	1.934	1350	2617	1.2
192	2.060	1.683	1103	2316	1.3
253	2.254	1.886	1296	2955	1.4

[a] The error in measuring the Mach number, M_s, is typically 0.5%−1.0% at the one standard deviation level. [b] Quantities with the subscript 5 refer to the thermodynamic state of the gas in the reflected shock region. [c] The rate constants are derived as described in the text.

OH-Radical Calibration and Kinetics Analysis. In addition to the C_2H_5I/NO_2 method (reactions 1−3) for producing OH-radicals, experiments were also performed utilizing the H_2/O_2 branching chain oxidation. This latter method has already been used by a number of investigators for the same reason, namely, that $[OH]_\infty$ is completely specified by the thermochemistry if the density, mole fraction of reactants, and temperature are known.[32−42] The mechanism for the H_2/O_2 reaction was taken mostly from an evaluation from this laboratory[21] that included the most recent direct determinations of the important rate constants. The details of these experiments and the results have been given previously.[23]

The C_2H_5I/NO_2 method can be illustrated by considering the kinetics experiment of Figure 2. In all kinetics experiments, $[NO_2]_0/[C_2H_5I]_0 \cong 2$, and therefore, simulations will be required. The top panel of Figure 2 shows a typical transmittance plot, $T = (I_t/I_0)$ against time. After conversion to $(ABS)_t \equiv -\ln(I_t/I_0)$ against time plots, the derived values at long times are compared to chemical simulations using the mechanism of Table 2. Because all rate constants except that of reaction 1 are known, a scale factor between the experimental values of (ABS) and the simulated values of [OH] is determined for varying values of k_1. This scale factor is the product of the effective cross section for absorption and the path length, that is, $\sigma_{eff}l$. In addition, we performed fourteen experiments (not shown) with $[NO_2]_0/[C_2H_5I]_0 \cong 10$. Hence, the simulated [OH] becomes

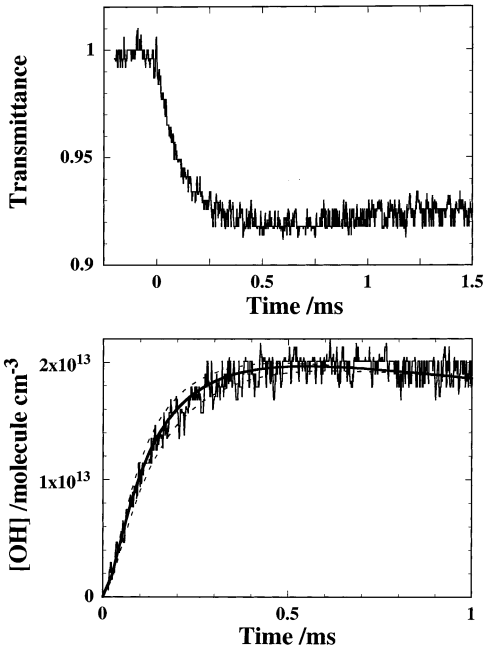

Figure 2. (top) OH-radical transmittance against time for an experiment at $T_5 = 1313$ K, $P_5 = 376$ Torr, and $\rho_5 = 2.764 \times 10^{18}$ cm^{-3} with $[C_2H_5I]_0 = 2.559 \times 10^{13}$ cm^{-3} and $[NO_2]_0 = 4.770 \times 10^{13}$ cm^{-3} and (bottom) OH-radical profile derived from the transmittance record (top) using the curve-of-growth expression, eq 5. The solid line is a simulation based on the mechanism of Table 2 with $k_1 = 2.1 \times 10^{-10}$ cm^3 molecule^{-1} s^{-1}. The dashed lines are predicted profiles with k_1 varied by ±20%.

TABLE 2: Reaction Mechanism Used for Determining the Rate Constant for H + NO_2 Using C_2H_5I as a Source of H-atoms[a]

1.	$H + NO_2 \rightarrow OH + NO$, k_1 = to be fitted
2.	$OH + OH \rightarrow O + H_2O$, $k_2 = 7.19 \times 10^{-21} T^{2.7} \exp(1251/T)$[b]
3.	$C_2H_5I(+M) \rightarrow C_2H_4 + H + I(+M)$, $k_3 = 6.34 \times 10^9 \exp(-15\,894\ \mathrm{K}/T)$[c]
4.	$C_2H_5I + M \rightarrow C_2H_4 + HI + M$, $k_4 = 0.15 k_3$[c]
5.	$H + HI \rightarrow H_2 + I$, $k_5 = 7.87 \times 10^{-11} \exp(-330\ \mathrm{K}/T)$[d]
6.	$NO_2 + M \rightarrow NO + O + M$, $k_6 = \rho(1.96 \times 10^{-8}) \exp(-33\,162\ \mathrm{K}/T)$[e]
7.	$O + NO_2 \rightarrow NO + O_2$, $k_7 = 6.5 \times 10^{-12} \exp(120\ \mathrm{K}/T)$[f]

[a] All rate constants are in cm^3 molecule^{-1} s^{-1} except reactions 3 and 4, which are in s^{-1}. [b] Reference 21. [c] Reference 31. [d] Reference 43. [e] ρ refers to total density, ref 44. [f] Reference 45.

nearly independent of the rate constant for reaction 1 because the process then gives nearly instantaneous OH-radical production. The H_2/O_2 experiments were also analyzed by comparing $(ABS)_t$ to simulations.[23] We combined all three sets of data giving a database of 54 experiments. The dependence of (ABS) on total density, [OH], and temperature was determined.[23] This method of empirically determining the curve of growth under conditions that are to be used in the kinetics experiments has already been used by a number of researchers.[37−39,41] Using the three types of experiments, we found that (a) (ABS) was independent of density between 0.76×10^{18} and 5.6×10^{18} molecules cm^{-3}, (b) it is slightly dependent on temperature, and (c) it is not linearly dependent on [OH]. Within a 2σ error of ±25% (i.e., 95% confidence), the results can be represented by the modified Beer's law expression,

$$(\mathrm{ABS}) = 4.599 \times 10^{-12} T^{-0.443} [\mathrm{OH}]^{0.8757} \qquad (5)$$

where [OH] is in molecular units and $1250 \le T \le 2050$ K. Figure 3 shows an experimental plot of $(ABS)T^{0.443}$ against [OH] along with the line determined from eq 5. Note that this result

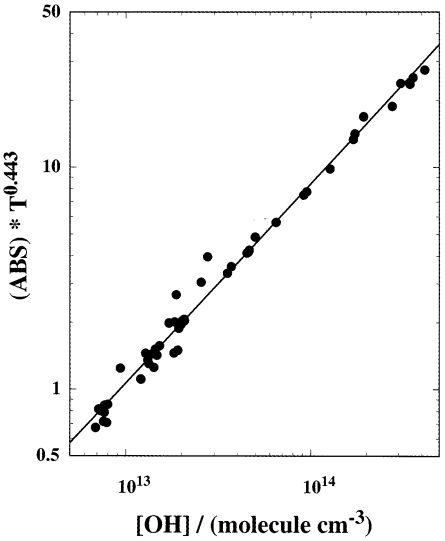

Figure 3. OH-radical absorption curve of growth derived as described in the text. The line is calculated from eq 5.

is slightly different from that given previously[23] because earlier and less reliable values for both the rate constant for reaction 2a and the branching ratio between reactions 2a and 2b were used.

Implicit in the determination of the scale factors from the C_2H_5I/NO_2 method is the specification of the rate constant values for reaction 1. When sufficiently low $[NO_2]_0$ is used, temporal resolution of $[OH]_t$ is possible. With the use of eq 5 to transform the (ABS) data to an OH-radical profile, the value for k_1 can be iteratively varied in a simulation until the best fit with experiment is obtained. The bottom panel of Figure 2 shows the method, giving $k_1 = 2.1 \times 10^{-10}$ cm^3 molecule^{-1} s^{-1} for the experiment. It is important to note that the substantial gain in OH-radical sensitivity with the multipass technique allows for reaction 1 to be studied under conditions in which secondary reaction perturbations are almost absent. In Figure 2, the minor long time decrease in [OH] is due to small effects from reaction 2 in Table 2; that is, OH + OH → H_2O + O. The dashed lines show similarly calculated profiles with a ±20% variation in the assumed k_1 value. A total of 26 experiments were carried out under the conditions given in Table 3, and ±20% is a typical error for the rate constants listed in the table. The combined rate constant results again show that there is no discernible temperature dependence. The data can be best represented as the constant value

$$k_1 = (1.8 \pm 0.2) \times 10^{-10}\,\mathrm{cm^3\ molecule^{-1}\ s^{-1}} \quad \text{for} \quad 1250 \le T \le 2000\ \mathrm{K} \qquad (6)$$

where the error is at the one standard deviation level. Comparing the H-atom depletion results, eq 4, to eq 6 shows that there may be a systematic difference between the two sets. Nevertheless, the values do in fact overlap within one standard deviation limits, and therefore, we have combined the two sets and report as the best representation

$$k_1 = (1.64 \pm 0.30) \times 10^{-10}\,\mathrm{cm^3\ molecule^{-1}\ s^{-1}} \quad \text{for} \quad 1100 \le T \le 2000\ \mathrm{K} \qquad (7)$$

Discussion

The present results can be compared to those from earlier studies. The data have been thoroughly reviewed by Michael et al.,[7] Ko and Fontijn,[9] and in the NIST kinetics database.[46] In

TABLE 3: High-Temperature Rate Data for H + NO_2 → OH + NO Using OH-Radical Detection

P_5[b] (Torr)	M_s[a]	ρ_5[b] (10^{18} cm^{-3})	T_5[b] (K)	k_1[c] (10^{-10} cm^3 s^{-1})
$X_{C_2H_5I} = 9.258 \times 10^{-6}$, $X_{NO_2} = 1.726 \times 10^{-5}$				
297	2.385	2.005	1432	2.1
356	2.545	2.127	1617	2.2
474	2.847	2.302	1990	1.6
397	2.646	2.196	1744	1.5
337	2.492	2.090	1556	2.0
272	2.314	1.930	1359	1.5
131	2.217	1.008	1258	1.5
174	2.449	1.113	1507	1.7
201	2.582	1.166	1666	1.9
226	2.691	1.217	1793	1.9
170	2.428	1.107	1483	1.9
143	2.288	1.037	1336	2.0
386	2.293	2.771	1343	1.7
479	2.477	3.000	1541	1.6
566	2.635	3.182	1716	1.5
536	2.582	3.131	1654	1.5
376	2.268	2.764	1313	2.1
434	2.392	2.907	1443	1.6
$X_{C_2H_5I} = 8.484 \times 10^{-6}$, $X_{NO_2} = 1.966 \times 10^{-5}$				
466	2.456	2.977	1513	2.0
373	2.589	2.156	1670	2.0
328	2.476	2.054	1544	1.8
301	2.397	2.006	1449	1.8
240	2.219	1.842	1260	1.5
366	2.249	2.730	1293	1.9
392	2.308	2.798	1354	1.7
430	2.383	2.906	1429	1.9

[a] The error in measuring the Mach number, M_s, is typically 0.5%−1.0% at the one standard deviation level. [b] Quantities with the subscript 5 refer to the thermodynamic state of the gas in the reflected shock region. [c] The rate constants represent best fits to experimental profiles using the reaction scheme listed in Table 2.

two of the earlier studies,[4,5] a relatively strong temperature dependence was suggested; however, the more recent studies disagree with this claim.[7,9] These latter studies used both the flash photolysis−resonance fluorescence, FP−RF (and its high-temperature modification, HTP[9]), and discharge flow−resonance fluorescence, DF−RF, techniques.[7] Hence, the results were obtained over large ranges of both temperature and density. It seems clear that the earlier claims of a strong temperature dependence are not correct; however, Ko and Fontijn[9] do suggest a moderate effect, reporting

$$k_1 = 2.15 \times 10^{-10} \exp(-182\ \mathrm{K}/T)\ \mathrm{cm^3\ molecule^{-1}\ s^{-1}} \quad (8)$$

for $296 \le T \le 760$ K. The present result, eq 7, can be compared to the values implied by eq 8. Our result overlaps the range of values calculated by eq 8 within experimental error. We conclude that if the earlier data with corresponding errors are taken into account then temperature dependence is clearly indeterminate. If a barrier exists for reaction 1, it is <100 cal mol^{-1}. Michael et al. report (1.41 ± 0.26) for 195−400 K,[7] Wategaonkar and Setser report 1.49 at 296 K,[8] Ko and Fontijn's average value is (1.41 ± 0.23) for 296−760 K,[9] and the present value is (1.64 ± 0.30) for 1100−2000 K, all in units of 10^{-10} cm^3 molecule^{-1} s^{-1}. If the studies are weighed according to the standard deviations, then the best representation for the entire temperature range, 195−2000 K, is

$$k_1 = (1.47 \pm 0.26) \times 10^{-10}\ \mathrm{cm^3\ molecule^{-1}\ s^{-1}} \quad (9)$$

This expression and the above-mentioned data are shown as an Arrhenius plot in Figure 4.

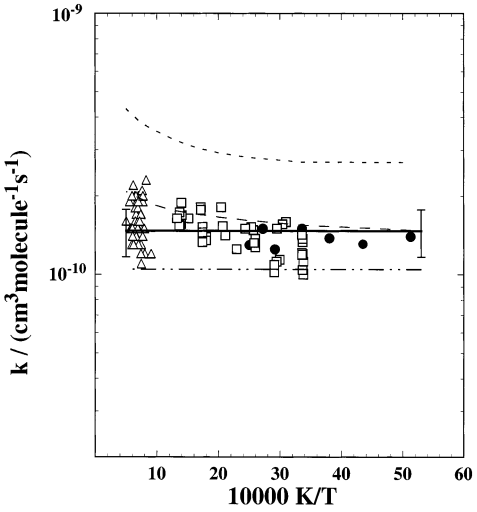

Figure 4. Arrhenius plot of experimental and theoretical data. Experiments include (△) present results, (●) Michael et al., ref 7, and (□) Ko et al., ref 9. The line (−) with error bars represents the combined experimental fit (eq 9). Theoretical results include (− − −) VRC−FTST calculations, (- - -) calculations of the Lennard-Jones model, and (−••) calculations of Nyugen et al., ref 54.

Theory. The rate behavior for reaction 1, eq 9, is ultra-simple, and the question arises as to whether such behavior is consistent with chemical kinetics theory. In earlier work,[7] it was shown that the rate constants were closely similar to the collision rate using a Lennard-Jones model; that is, the collision rate between H and NO_2 is calculated from the standard expression[47] for collisions under a Lennard-Jones interaction potential:

$$k_{LJ} = \left(\frac{g^{\ddagger}}{g_1 g_2}\right) {\sigma_{12}}^2 \Omega(2,2)^* \left(\frac{8\pi kT}{\mu}\right)^{1/2} \exp\left(\frac{\epsilon_{12}}{kT}\right) \quad (10)$$

where the ratio of electronic degeneracy factors, g, is $^1/_4$. The interaction potential parameters σ and ϵ for both H and NO_2 are derived from polarizabilities (by methods described in Hirschfelder, Curtiss, and Bird[47]) as suggested by Cambi et al.[48] and combined as in that reference to obtain σ_{12} and ϵ_{12} for use in the above equation. We obtain $\sigma_{H,NO_2} = 3.416$ Å and $\epsilon_{H,NO_2} = 64.135$ K, which give values for the collision rate ranging from 2.7×10^{-10} to 4.3×10^{-10} cm^3 molecule^{-1} s^{-1} for 195−2000 K. These results are plotted in Figure 4 and are approximately 2−2.5 times larger than the measurements. Because this model involves many assumptions, more detailed theoretical calculations are called for. We have accordingly considered this system by first determining the ab initio potential energy surface (PES) for the interaction and then applying flexible transition state theory (FTST)[49] to calculate the temperature dependence and rate behavior.

Selected portions of the HNO_2 PES have already been studied by others.[50−54] Of these, the most relevant study is that of Nguyen et al.[54] They used B3LYP density functional theory (DFT), quadratic configuration interaction singles and doubles with triples correction (QCISD(T)), and coupled cluster singles and doubles with triples correction (CCSD(T)) electronic structure calculations to map out the four isomers (HNO_2, HONO, HNOO, and $H(NO_2)_{triangle}$) and the reaction pathways that connect them to each other and to the possible low-lying asymptotes (H + NO_2, OH + NO, and NH + O_2). Their results show that there are barrierless reaction pathways that directly connect the reactants H + NO_2 to either isomer HONO or HNO_2. H + NO_2 collisions that lead directly to HONO complexes quickly undergo decomposition to OH + NO

TABLE 4: Computed versus Experimental Properties for NO_2

	R_{NO} (Å)	∠ONO (degree)	asym. stretch (cm^{-1})	sym. stretch (cm^{-1})	bend (cm^{-1})
theory	1.1826	135.2	1867	1514	798
experiment[a]	1.1934	134.1	1618	1320	750

[a] Reference 58.

products (with an exothermicity of ~30 kcal mol^{-1} relative to the reactant asymptote). However, any HNO_2 complex formed has no energetically accessible reaction paths directly to products. Instead, it must first isomerize to HONO, which then decays to products. Nguyen et al. calculate that the isomerization barrier is about 20 kcal mol^{-1} below the reactant H + NO_2 asymptote, implying a facile isomerization. Indeed, their reaction rate calculations (to be discussed later) show that this is so. This is also consistent with the suggestion that the HONO complex lifetime is less than one rotational period and probably the same order of magnitude as that for a vibration.[18] Thus, in the context of the present experiments, the theoretical results of Nguyen et al. confirm that the rate-limiting step to the loss of reactant H or the formation of product OH is the total rate of complex formation from the reactants H + NO_2. Only at much higher pressures than are experimentally sampled do the details of the decay routes of the HONO and HNO_2 complexes become important.

Nyugen et al. did not choose to study in detail the reaction pathways that lead H + NO_2 to either complex. Consequently, we have carried out new electronic structure calculations to survey enough of the PES to describe the reaction paths and the dependence of the energy on three conserved and two transitional degrees of freedom that describe deviations from the path. The meaning of "conserved" and "transitional" are in the FTST sense: conserved degrees of freedom are vibrations found in both the H + NO_2 reactants and either complex while transitional degrees exist as free rotations in the reactants but vibrations in the complexes. Transitional degrees of freedom can display large amplitude, anharmonic motion away from the reaction path and therefore can require the characterization of a substantial portion of the PES.

Although NO_2 is a stable gas, it has a radical character, and the H-atom radical and the radical nature of the H + NO_2 reaction accounts for its barrierless reaction paths to either complex. Long-range potential surfaces for radical−radical interactions are poorly described by single reference methods. For this reason a multireference, singles and doubles, configuration interaction (MRSDCI) approach was used in the present work. The reference space for the MRSDCI calculations was a two electron−two orbital, complete active space, self-consistent field wave function (CASSCF) in which the two active orbitals are the two single occupied radical orbitals of the reactants. This is the minimum reference space needed to allow for a correct (i.e., not spin-contaminated) description of the reactants. The calculations employed the correlation-consistent, polarized double-ζ (cc-pvdz) basis set of Dunning,[55] which is similar in size to that used by Nyugen et al. All calculations were carried out using the MOLPRO program package.[56,57] In Table 4, the computed properties of NO_2 at the H + NO_2 asymptote are compared to experiment.[58] As the table shows for structural properties, the computed bond angle and R_{NO} distance are 1.1° and 0.01 Å too small, respectively. The computed frequencies are 48, 194, and 249 cm^{-1} too high relative to *anharmonic* experimental frequencies[58] for the bend, symmetric stretch, and asymmetric stretch, respectively.

Before describing the results of the electronic structure calculations, a brief description of coordinates appropriate for the H + NO_2 complex formation reaction is required. Beyond the separation coordinate between the two reactants that measures progress along the reaction path, the PES is a function of five other coordinates. Of these five, it is the variation of the potential energy with the two transitional coordinates and how that variation changes as a function of the separation coordinate that has the most impact on the rate constant. These two transitional coordinates can be described in terms of the spherical (θ) and azimuthal (ϕ) angles of a spherical coordinate system of which the z axis is the C_{2v} axis of NO_2 ($+z$ pointing away from bent NO_2) and of which the origin is the N atom. The remaining three coordinates describe the bend, asymmetric stretch, and symmetric stretch of NO_2. The separation coordinate can be measured in terms of the R_{NH} distance.

In terms of these coordinates, the electronic structure calculations can ideally provide the structure and energetics as a function of R_{NH} along the reaction paths, the three conserved vibrational frequencies as a function of R_{NH} along the reaction paths, and the interaction potential $V(\theta,\phi,R_{NH})$ with NO_2 fixed at its reaction path structure for R_{NH}. For the H + NO_2 reaction, all reaction paths have H in the NO_2 plane. In the kinetically important regions of the reaction path, the structure of NO_2 differs marginally from the equilibrium structure (R_{NO} = 2.25 a_0, ∠ONO = 135°). Thus, as a minor approximation, the equilibrium geometry of NO_2 was presumed to describe the NO_2 geometry in calculations defining $V(\theta,\phi,R_{NH})$. Under these circumstances, as a function of ϕ, $V(\theta,\phi,R_{NH})$ has unique values only over the range 0°−90°.

Because of the location of the reaction paths, most of the electronic structure calculations sampled that portion of the PES in which the H atom lies in the plane of the NO_2. With the NO_2 frozen at its equilibrium geometry, R_{NH} was varied over an unevenly spaced grid of 24 points from 3.5 to 9.0 a_0, and the angle of H with respect to the C_{2v} axis of NO_2 was varied over an unevenly spaced grid of 49 points from 0° to 180°. The resulting 1176 ab initio energies were fit to a 2D spline to produce $V(\theta,\phi=0,R_{NH})$ as displayed in Figure 5a. The bands in the figure represent 2 kcal mol^{-1} increments with the light and dark bands at the largest value of R_{NH} representing the increment just below or just above 0 kcal mol^{-1}, respectively. By definition of θ, 0° corresponds to H approaching the "frontside" of N along the C_{2v} axis (the two O atoms point away from the H) while 180° corresponds to the H approaching the "backside" of N. The figure shows that both approaches are attractive. An H attack along the extension of the N−O axis would occur at θ = 112.5°, but the figure shows that that approach is repulsive. At angles intermediate between θ = 112.5° and 180°, there is an attractive approach. Furthermore, inside a 20 kcal mol^{-1} barrier at close-in values of R_{NH}, there is also an attractive approach at angles intermediate between θ = 0° and 112.5°. NO_2 has p orbital radical character in the plane on both the N and the O atoms. Just as the H can access both the frontside and backside of the p orbital on the N, it can do the same for the O with the only attractive access being the backside attack of the O. Thus, in this (θ,R_{NH}) portion of the PES, there are four reaction paths to complex formation, two of which involve barrierless H attack on the N and two of which involve H attack on the O. There are three saddle points in the figure, one for the H attack on the O, which has a barrier, one connecting the two O attack reaction paths, and one connecting the two reaction pathways involving H attack on the backside of O or N. From a thermal kinetics point of view, the frontside attack of O over

a ~20 kcal mol^{-1} barrier cannot compete with the other barrierless reaction paths and can be ignored.

No electronic structure calculations were done to systematically explore the ϕ dependence of $V(\theta,\phi,R_{NH})$. Rather the following approximations were used. At $\phi = 90°$, H moves on the plane that perpendicularly bisects the NO_2. Because the radical p orbital of each O atom lies in the NO_2 plane and is largely aligned parallel to the perpendicularly bisecting plane, it is unlikely that any attractive trace of the reaction paths for H attack on the O atoms will be found in $V(\theta,\phi{=}90°,R_{NH})$. However, because the radical p orbital on the N atom lies along the C_{2v} axis, both frontside and backside H attack on the N will be present but modified. In the terminology of nonbonded and bonded interactions, at $\phi = 90°$, only the nonbonded and the N−H bonded interactions will be important while the bonded O−H interactions that are obvious in Figure 5 for $\phi = 0°$ will be negligible. The modifications to the H attack on N will occur only because the nonbonded interactions of H with O will be different because the R_{OH} distances will be different. This analysis suggests the following approximation for $V(\theta,\phi,R_{NH})$:

$$V(\theta,\phi,R_{NH}) = V(\theta,\phi{=}0°,R_{NH})\cos^2\phi + V_{app}(\theta,R_{OH},R_{O'H},R_{NH})(1-\cos^2\phi) \quad (11)$$

where V_{app} has an argument list appropriate for nonbonded and N−H bonded interactions and where $\cos^2\phi$ acts as a switch to turn on V_{app} for deviations out of the four atom plane.

Through the use of typical representations of bonded and nonbonded interactions, V_{app} can take the form

$$V_{app}(\theta,R_{OH},R_{O'H},R_{NH}) = V_{NH}(R_{NH})\cos^2\theta + V_{nonbond}(R_{OH},R_{O'H},R_{NH})(1-\cos^2\theta) \quad (12)$$

In this form, $\theta = 0°$ or 180° leaves only the V_{NH} term, which therefore corresponds to frontside or backside attack attack on N by H. Hence,

$$V_{NH}(R_{NH}) = V(\theta,\phi{=}0°,R_{NH}) \quad \text{for} \quad \theta = 0°, 180° \quad (13)$$

If one assumes that bonding interactions between H and either O for $\phi = 0°$ is negligible for $\theta \le 90°$, then

$$V_{nonbond}(R_{OH},R_{O'H},R_{NH})|_{\phi=0°} = [V(\theta,\phi{=}0°,R_{NH}) - V_{NH}(R_{NH})\cos^2\theta]/(1-\cos^2\theta) \quad (14)$$

The $\phi = 0°$ constraint is imposed on the LHS of eq 14 because R_{OH} and $R_{O'H}$ depend on ϕ for a given θ and R_{NH}. What is needed is a parametrized functional form for $V_{nonbond}$ that is a function of the distance arguments without any ϕ constraint but the parameters of which are set to minimize divergence from the equality of eq 14. The form finally adopted is

$$V_{nonbond}(R_{OH},R_{O'H},R_{NH}) = A(e^{-\alpha R_{OH}} + e^{-\alpha R_{O'H}}) + B(e^{-2\alpha R_{OH}} + e^{-2\alpha R_{O'H}}) + C(R_{NH}) \quad (15)$$

where a common A, B, and α are fit for all R_{NH} but C is optimized at each R_{NH} value. $C(R_{NH})$ has a largely exponential character but is exactly represented as an exponential spline of R_{NH}. As Figure 5a indicates, for $R_{NH} \le \sim 5\ a_0$ and $\theta \ge \sim 50°$, bonding components for the frontside attack of H on O become prominent and were therefore excluded from the fits. The final fitting error of the RHS of eq 15 to the RHS of eq 14 is only 0.3 kcal mol^{-1}. Given the optimized values of A, B, $C(R_{NH})$, and α, $V_{nonbond}$ is determined, which together with V_{NH} of eq 13 determines V_{app} of eq 12 and hence $V(\theta,\phi,R_{NH})$ via eq 11 for any kinetically relevant values of its arguments.

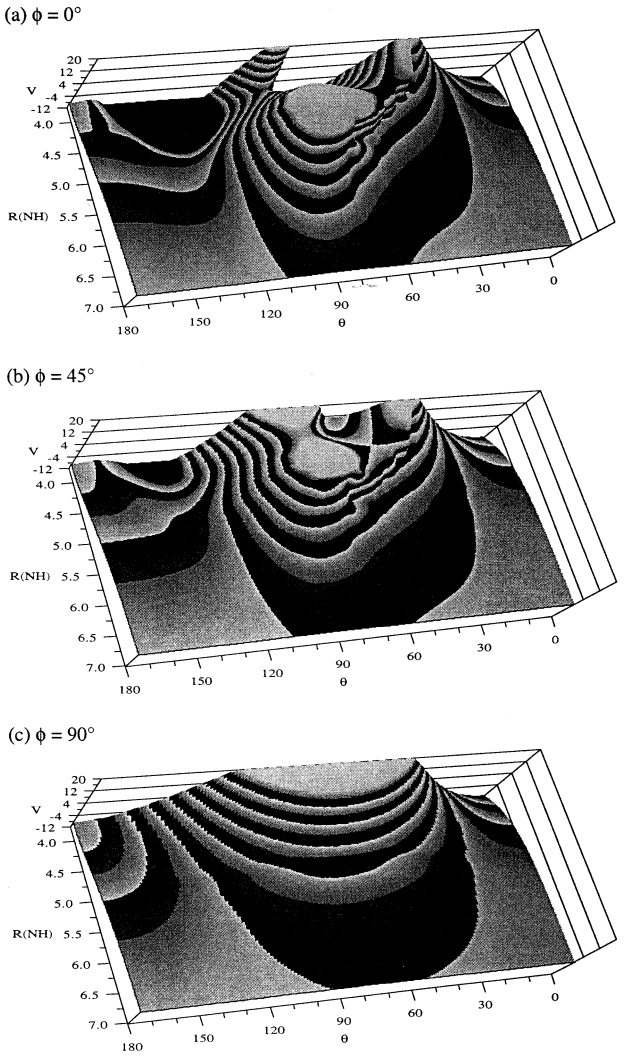

Figure 5. $V(\theta,\phi,R_{NH})$ in kcal mol^{-1} as a function of θ (deg) and R_{NH} (a_0) for $\phi = 0°$ (a), $\phi = 45°$ (b), and $\phi = 90°$ (c). Each band in the figure represents 2 kcal mol^{-1}. At the largest values of R_{NH}, the zero contour separates the dark and the light band. Where $V(\theta,\phi,R_{NH})$ is lower than −12 kcal mol^{-1}, the potential is represented by a dark floor. Where $V(\theta,\phi,R_{NH})$ is higher than 20 kcal mol^{-1}, the potential is represented by a light plateau.

Figure 5c displays $V(\theta,\phi{=}90°,R_{NH})$ from the same perspective as Figure 5a. From eq 11, $V(\theta,\phi{=}90°,R_{NH})$ is exclusively due to V_{app}. Only the attraction to either side of the N atom remains in the figure; all trace of H attack on O has disappeared because of repulsive interactions. Figure 5b displays $V(\theta,\phi{=}45°,R_{NH})$, which is intermediate in character between the interaction potential for $\phi = 0°$ (Figure 5a) and $\phi = 90°$ (Figure 5b). Because Figure 5 parts b and c do not represent any electronic structure calculations except along the two reaction paths involving N attack by H, the final $V(\theta,\phi,R_{NH})$ used in the kinetics calculations is qualitatively correct but probably not quantitatively correct in detail away from the four atom plane. As will be discussed later, it is unlikely that an ab initio map of the PES like that of Figure 5 only for other values of ϕ would have an important impact on the computed rate constants.

While $V(\theta,\phi,R_{NH})$ gives the effect of transitional mode deviations from the path, there is no information about the change in vibrational frequencies for conserved modes or about the distortion of NO_2 from its equilibrium geometry with

progress along the reaction path. (For $V(\theta,\phi,R_{NH})$, NO_2 was held at its asymptotic geometry.) That information was calculated for the reaction paths involving H attack of the frontside of N and of the backside of O, the two most prominent reaction paths for $V(\theta,\phi=0°,R_{NH})$. In these calculations, all degrees of freedom were allowed to relax to produce the full dimensional paths. As will be discussed shortly, the kinetically important region of the reaction paths corresponds to separations of H from the center-of-mass of NO_2 of $\geq\sim5$ a_0. For H attack on N, over this region, the NO_2 is essentially unchanged and all of the conserved vibrational frequencies increase but by less than 25 cm^{-1} (in the largest frequency, the asymmetric stretch). The change in zero-point energy is always less than about 0.06 kcal mol^{-1}. For H attack on O, the geometry of NO_2 also remains unchanged. The same general behavior of the frequencies remains true for center-of-mass separations greater than $\sim$5.5 a_0. Over this region, no frequency changes by more than ±10 cm^{-1} and the change in the zero-point energy is always less than 0.05 kcal mol^{-1}. For separations between 5.0 and 5.5 a_0, one frequency, the symmetric stretch, increases by $\sim$125 cm^{-1} while the other two increase by 25−50 cm^{-1}, resulting in a zero-point energy increase of 0.3 kcal mol^{-1}. At these close distances, the separability of the transitional and conserved degrees of freedom is beginning to breakdown. However, the breakdown is relatively small and, as will be discussed, applies to only the highest temperature portion of the rate constant. Given the approximations already in $V(\theta,\phi,R_{NH})$, the variation in the conserved vibrational frequencies along each reaction path and between reaction paths was ignored.

Given the computed structure and frequencies of the NO_2, the approximation that the structure and conserved frequencies change negligibly along the reaction paths, and the computed interaction potential $V(\theta,\phi,R_{NH})$ for the transitional degrees of freedom, a FTST calculation can be performed. The freeware code VariFlex was used[59] in this calculation. FTST calculations are generally variational in that the minimum rate constant as a function of progress along the reaction path is the most accurate estimate (because it minimizes recrossing effects). In addition to the usual variational options, VariFlex has a variable reaction coordinate (VRC) option, which permits additional minimization of the rate constant by varying the description of the reaction coordinate. This option requires, at each distance along the reaction path, a search for the optimal pivot point for NO_2 about which the two transitional degrees of freedom are executed. VariFlex also allows canonical or microcanonical calculations. At the microcanonical level, optimization of the reaction path and the position on the path takes places at each point on a grid of total energy and total angular momentum that spans the range that contributes significantly to the thermal rate constant over the temperatures of interest. At the canonical level, variational studies are carried out only for each temperature.

In Figure 4, the results of a canonical VRC−FTST rate constant calculation are displayed relative to the measurements reported here, to the two previous measurements, and to other calculations or fits. VRC effects are minor; a rate constant, determined with a center-of-mass separation distance as the definition of the reaction path, would be no more than 10% higher than that in the figure. However, as expected the location of the reaction bottleneck does decrease with temperature. When expressed in terms of the center-of-mass separation distance, the location varies from 7.0 a_0 at 200 K to 5.5 a_0 at 1100 K to 4.9 a_0 at 2000 K. This confirms that the small breakdown in the separation between conserved and transitional degrees of freedom discussed above will only affect the highest temperatures. Microcanonical effects were found to be minor. With the center-of-mass definition of the reaction coordinate, microcanonical and canonical rate constants are the same within the 2−3% integration error.

The reliability of the VRC−FTST calculations in Figure 4 depends in part on the accuracy of the computed PES which, as discussed above, contains approximations. To gauge the sensitivity of the computed rate constants to the PES, several FTST calculations were performed on distorted representations of $V(\theta,\phi,R_{NH})$. In these calculations, for simplicity, the pivot point for the transitional modes of motion was fixed at the center of mass of NO_2. A $\pm30\%$ variation in the size of $V_{nonbond}$ [see eq 15] results in at most a $\pm10\%$ variation in the computed rate constant over the 200−2000 K temperature range. The use of a $\cos^4\phi$ switching function in eq 11 resulted in less than a 5% variation in the computed rate constant. These calculations indicate that relatively substantial changes in those portions of the PES that are approximated do not lead to substantial changes in the results displayed in Figure 4.

Another source of uncertainty in the VRC−FTST calculations comes from symmetry number assignments. At a fixed distance of H from the center of mass of NO_2 (the optimal pivot point for the VRC−FTST calculations), the reaction path energy for N attack is always more attractive than the reaction path energy for O attack in the reaction bottleneck region. Thus, the reaction path for O attack can be considered simply a feature on the hindered rotation potential for the reaction path for N attack. Because that reaction path has a C_{2v} geometry, the symmetry number should be 2, and the calculations in Figure 4 are with this assignment. However, the appropriate method for assigning symmetry numbers for a theory that rigorously classically incorporates large amplitude internal motion and external rotational motion is unclear. In this case, the reaction path energy for O attack is not that much less attractive ($\sim1\%-30\%$) than that for N attack and has a larger range of angles for which the PES is substantially attractive. A typical harmonic-oscillator approach to $H + NO_2$ would have two reaction paths, one for N attack (symmetry number of 2) and one for O attack (symmetry number of 1). For these reasons, an alternative VRC−FTST model was studied in which parts of the PES away from the region about each atom in NO_2 were masked by a uniformly high repulsive potential. This PES decomposition is somewhat arbitrary but leads to a decomposition of the rate into a part that goes to HNO_2 (assigned a symmetry number of 2) and a part that goes to HONO (assigned a symmetry number of 1). Furthermore, with the PES decomposed, the pivot point for the attack on each atom can be separately optimized. This alternative VRC−FTST calculation produces rate constants approximately 50%−60% larger than the VRC−FTST rate constants shown in Figure 4. This 50%−60% variation represents the range of symmetry number treatments possible for $H + NO_2$ within the context of FTST and is the largest uncertainty in the calculation. The model used in Figure 4 is selected because it is the simpler one and more consistent with experiment. In the future, more analysis of the implications of reaction path symmetry is required for theories such as FTST that directly incorporate large amplitude motion. As an aside, the alternative VRC−FTST calculations produce rate constants noticeably lower than, but somewhat similar to, the Lennard-Jones rate constants in Figure 4. This suggests that the Lennard-Jones model is too high not only because its potential is too simple but also because its spherically symmetric PES about

each reactant is only consistent with a symmetry number of unity.

As already discussed, the solid flat line with the error bars in Figure 4 is the best representation of the experimental results over 195−2000 K. The calculated VRC−FTST results are not flat but show an increase with temperature. While the computed rate constants are always above the best experimental representation, these calculations are never more than about 40% higher and are not inconsistent with the original experimental data. They are in noticeably better agreement with experiment than the simple Lennard-Jones model of eq 10 discussed above.

The VRC−FTST rate constants are about a factor of 1.5−2.0 higher than the calculated rate of Nguyen et al. that tends to lie below most of the measurements. In calculating their rate constant, Nyugen et al. used canonical variational transition state theory applied separately to the two reaction paths for H attack on the frontside of N and on the backside of O. With either path, harmonic energy changes are assumed for deviations perpendicular to the path in all five available degrees of freedom. Each path was determined with a B3LYP density functional theory calculation, followed by a QCISD(T) refinement of the energy on the B3LYP path, followed by a fit of the energy variation along the path to a Morse oscillator functional form. The variational location of the reaction bottleneck was carried out on this Morse form and the resulting final rate constant was then fit to a single exponential form. The *A* factor of this fit is listed by Nguyen et al. for each path, but the activation energy is not. From the figures in the Nguyen et al. study, the rate constant temperature dependence and hence the activation energy is quite small and not resolvable on the scale of Figure 4. What is shown for Nguyen et al. in Figure 4 is the sum of the *A* factors alone with the activation energies being set to zero.

Conclusions

Rate constants for the reaction $H + NO_2 \rightarrow OH + NO$ have been measured over the temperature range of 1100−2000 K in reflected shock experiments. The source of H-atoms is from ethyl radical decomposition in which the radical is formed essentially instantaneously from the thermal decomposition of C_2H_5I. In one set of measurements, atomic resonance absorption spectrometry is used to follow the temporal behavior of H-atoms under conditions so dilute in $[C_2H_5I]$ that the $H + NO_2$ reaction could be chemically isolated with strictly first-order decay of H-atoms. In a second set of measurements, a multipass optical system for observing the product radical, OH, was used with a resonance lamp as an absorption source. Because this is the first OH-radical kinetics investigation from this laboratory, extensive calibration was performed to obtain the curve of growth that converts absorption data to OH-radical profiles. Rate constants by this method required chemical simulation. The results of both methods statistically overlap, combining to give $k = (1.64 \pm 0.30) \times 10^{-10}$ cm^3 molecule^{-1} s^{-1} for $1100 \leq T \leq 2000$ K. When combined with two earlier measurements at lower temperatures, the result is a temperature independent $k = (1.47 \pm 0.26) \times 10^{-10}$ cm^3 molecule^{-1} s^{-1} for 195−2000 K.

Several theoretical methods were applied to calculate this rate constant. The simplest method based on Lennard-Jones collsion rates could only estimate values to within about a factor of 2. The most sophisticated involved multireference configuration interaction calculation of that portion of the potential energy surface describing H approaching NO_2 in its equilibrium geometry. This portion of the surface was used in a variational reaction coordinate flexible transition state theory calculation of the rate constant. The resulting rate constant increases somewhat with temperature and is on the high side of the spread of measured data from this work and two other laboratories.[7,9] The computed rate is 1.5−2 times higher than the only other computed rate constant available in work by Nguyen et al.[54] The Nguyen et al. computed rate constant came from an application of canonical variational transition state theory to a fully harmonic description of the reaction paths calculated with different electronic structure methods than those employed here.

The convergence of measurements from three different laboratories and calculations with two different relatively high-level methods indicates that the rate constant for the $H + NO_2 \rightarrow OH + NO$ reaction has at best a weak temperature dependence and a value quite close to 1.5×10^{-10} cm^3 molecule^{-1} s^{-1}.

Acknowledgment. This work was supported by the U. S. Department of Energy, Office of Basic Energy Sciences, Division of Chemical Sciences, under Contract No.W-31-109-Eng-38.

References and Notes

(1) Rosser, W. A.; Wise, H. *J. Phys. Chem.* **1961**, *85*, 532, 2227.
(2) Ashmore, P. G.; Tyler, B. *J. Trans. Faraday Soc.* **1962**, *58*, 1108.
(3) Phillips, L. F.; Schiff, H. I. *J. Chem. Phys.* **1962**, *37*, 1233.
(4) Wagner, H. Gg.; Welzbacher, U.; Zellner, R. *Ber. Bunsen-Ges. Phys. Chem.* **1976**, *80*, 1023.
(5) Clyne, M. A. A.; Monkhouse, P. B. *J. Chem. Soc., Faraday Trans. 2* **1977**, *73*, 298.
(6) Bemand, P. P.; Clyne, M. A. A. *J. Chem. Soc., Faraday Trans. 2* **1977**, *73*, 394.
(7) Michael, J. V.; Nava, D. F.; Payne, W. A.; Stief, L. J. *J. Phys. Chem.* **1979**, *83*, 2818.
(8) Wategaonkar, S. J.; Setser, D. W. *J. Chem. Phys.* **1989**, *90*, 251.
(9) Ko, T.; Fontijn, A. *J. Phys. Chem.* **1991**, *95*, 3984.
(10) Anderson, J. G.; Kaufman, F. *Chem. Phys. Lett.* **1972**, *16*, 375. Anderson, J. G.; Margitan, J. J.; Kaufman, F. *J. Chem. Phys.* **1974**, *60*, 3310. Michael, J. V.; Keil, D. G.; Klemm, R. B. *J. Chem. Phys.* **1985**, *83*, 1630.
(11) Spencer, J. E.; Glass, G. P. *Chem. Phys.* **1976**, *15*, 35.
(12) Clyne, M. A. A.; Nip, W. W. In *Reactive Intermediates in the Gas Phase*; Setser, D. W., Ed.; Academic: New York, 1979; Chapter 1 and references therein.
(13) Maki, R. G.; Michael, J. V.; Sutherland, J. W. *J. Phys. Chem.* **1985**, *89*, 4815. Michael, J. V.; Lifshitz, A. In *Handbook of Shock Waves*; Ben-Dor, G., Igra, O., Elperin, T., Lifshitz, A., Eds.; Academic: New York, 2001; Chapter 16.3, pp 77−105.
(14) Polanyi J. C.; Sloan, J. J. *Int. J. Chem. Kinet.* **1975**, *7* (Suppl.), 51. Donaldson, D. J.; Wright, J. S.; Sloan, J. J. *Can. J. Chem.* **1983**, *61*, 91.
(15) Brophy, J. H.; Silver, J. A.; Kinsey, J. L. *J. Chem. Phys.* **1975**, *62*, 3820. Silver, J. A.; Dimpfl, W. L.; Brophy, J. H.; Kinsey, J. L. *J. Chem. Phys.* **1976**, *65*, 1811. Murphy, E. J.; Brophy, J. H.; Arnold, G. S.; Dimpfl, W. L.; Kinsey, J. L. *J. Chem. Phys.* **1981**, *74*, 324.
(16) Haberland, H.; Rohwer, P.; Schmidt, K. *Chem. Phys.* **1976**, *5*, 35. Haberland, H.; von Lucadou, W.; Rohwer, P. *Ber. Bunsen-Ges. Phys. Chem.* **1977**, *81*, 150; *Ber. Bunsen-Ges. Phys. Chem.* **1980**, *84*, 507.
(17) Wickramaaratchi, M. A.; Setser, D. W.; Hildebrandt, B.; Korbitzer, B.; Heydtmann, H. *Chem. Phys.* **1984**, *84*, 105.
(18) Sauder, D. G.; Dadigian, P. J. *J. Chem. Phys.* **1990**, *92*, 2389.
(19) Irvine, A. M. L.; Smith, I. W. M.; Tuckett, R. P.; Yang, X. F. *J. Chem. Phys.* **1990**, *93*, 3177. Irvine, A. M. L.; Smith, I. W. M.; Tuckett, R. P. *J. Chem. Phys.* **1990**, *93*, 3190.
(20) Miziolek, A. W.; Melius, C. F.; Thorne, L. R.; Dagdigian, P. J.; Alexander, M. H. *Gas-Phase Combustion Chemistry of Nitramine L. R.; Propellants*; Report BRL-TR-2906; Ballistic Research Laboratory: March, 1988.
(21) Michael, J. V. *Prog. Energy Combust. Sci.* **1992**, *18*, 327.
(22) For original references, see: Michael, J. V. In *Advances in Chemical Kinetics and Dynamics*; Barker, J. R., Ed.; JAI: Greenwich, CN, 1992; Vol. I, p 47.
(23) Su, M.-C.; Kumaran, S. S.; Lim, K. P.; Michael, J. V. *Rev. Sci. Instrum.* **1995**, *66*, 4649.
(24) Michael, J. V.; Sutherland, J. W. *Int. J. Chem. Kinet.* **1986**, *18*, 409.
(25) Michael, J. V. *J. Chem. Phys.* **1989**, *90*, 189.

(26) Michael, J. V.; Fisher, J. R. *AIP Conf. Proc. 208, 17th Int. Symp. Shock Waves Shock Tubes* **1990**, *17*, 210.

(27) Miller, J. C.; Gordon, R. J. *J. Chem. Phys.* **1983**, *78*, 3713.

(28) White, J. U. *J. Opt. Soc. Am.* **1942**, *32*, 285.

(29) Bernstein, H. J.; Herzberg, G. *J. Chem. Phys.* **1948**, *16*, 30.

(30) (a) Herzler, J.; Frank, P. *Ber. Bunsen-Ges. Phys. Chem.* **1992**, *96*, 1333. (b) Lim, K. P.; Michael, J. V. In *Twenty-Fifth Symposium (International) on Combustion*; The Combustion Institute: Pittsburgh, PA, 1994; p 713.

(31) Kumaran, S. S.; Su, M.-C.; Lim, K. P.; Michael, J. V. In *Twenty-Sixth Symposium (International) on Combustion*; The Combustion Institute: Pittsburgh, PA, 1996; p 605.

(32) See: Bird P. F.; Schott, G. L. *J. Quant. Spectrosc. Radiat. Transfer* **1965**, *5*, 783 and references therein. Schott, G. L.; Getzinger, R. W. In *Physical Chemistry of Fast Reactions*; Levitt, P. B., Ed.; Plenum: London, 1973; p 81.

(33) Gardiner, W. C., Jr.; Mallard, W. G.; Owen, J. H. *J. Chem. Phys.* **1974**, *60*, 2290.

(34) Bradley, J. N.; Capey, W. D.; Fair, R. W.; Pritchard, D. K. *Int. J. Chem. Kinet.* **1976**, *8*, 549.

(35) (a) Ernst, J.; Wagner, H. Gg.; Zellner, R. *Ber. Bunsen-Ges. Phys Chem.* **1977**, *81*, 1270. (b) Ernst, J.; Wagner, H. Gg.; Zellner, R. *Ber. Bunsen-Ges. Phys Chem.* **1978**, *82*, 409. (c) Niemitz, K. J.; Wagner, H. Gg.; Zellner, R. *Z. Phys. Chem.* **1982**, *NF124*, 155. (d) Lorenz, K.; Zellner, R. *Ber. Bunsen-Ges. Phys. Chem.* **1984**, *88*, 1228.

(36) (a) Hanson, R. K.; Salimian, S.; Kychankoff, G.; Booman, R. A. *Appl. Opt.* **1983**, *22*, 641. (b) Rea, E. C., Jr.; Chang, A. Y.; Hanson, R. K. *J. Quantum Spectrosc. Radiat. Transfer* **1987**, *37*, 117. (c) Masten, D. A.; Hanson, R. K.; Bowman, C. T. *J. Phys. Chem.* **1990**, *94*, 7119.

(37) (a) Bott, J. F.; Cohen, N. *Int. J. Chem. Kinet.* **1984**, *16*, 1557. (b) **1989**, *21*, 485. (c) **1991**, *23*, 1017. (d) **1991**, *23*, 1075.

(38) Yuan, T.; Wang, C.; Yu, C.-L.; Frenklach, M.; Rabinowitz, M. J. *J. Phys. Chem.* **1991**, *95*, 1258.

(39) Du, H.; Hessler, J. P. *J. Chem. Phys.* **1992**, *96*, 1077.

(40) Frisch, S.; Hippler, H.; Troe, J. *Combust. Flame* **1994**, *99*, 254.

(41) (a) Fujii, N.; Shin, K. S. *Chem. Phys. Lett.* **1988**, *151*, 461. (b) Yang, H.; Gardiner, W. C., Jr.; Shin, K. S.; Fujii, N. *Chem. Phys. Lett.* **1994**, *231*, 449.

(42) Ryu, S.-O.; Hwang, S. M.; Rabinowitz, M. J. *J. Phys. Chem.* **1995**, *99*, 13984.

(43) Baulch, D. L.; Duxbury, J.; Grant, S. J.; Montague, D. C. *J. Phys. Chem. Ref. Data* **1981**, *10* (Suppl. 1), 1-1.

(44) Hiraoka H.; Hardwick, R. *J. Chem. Phys.* **1963**, *39*, 2361.

(45) Atkinson, R.; Baulch, D. L.; Cox, R. A.; Hampson, R. F., Jr.; Kerr, J. A.; Troe, J. *J. Phys. Chem. Ref. Data* **1992**, *21*, 1125.

(46) Westley, F.; Frizzell, D. H.; Herron, J. T.; Hampson, R. F.; Mallard, W. G. *NIST Chemical Kinetics Database*, version 5.0; NIST Standard Reference Database 17; National Institute of Standards and Technology: Gaithersburg, MD, 1993.

(47) Hirschfelder, J. O.; Curtiss, C. F.; Bird, R. B. *Molecular Theory of Gases and Liquids*; Wiley: New York, 1966.

(48) Cambi, R.; Cappelletti, D.; Liuti, G.; Pirani, F. *J. Chem. Phys.* **1991**, *95*, 1852.

(49) Robertson, S.; Wagner, A. F.; Wardlaw, D. M. *J. Chem. Phys. A* **2000**, *113*, 2648 and references therein.

(50) Nakamura, S.; Takahashi, M.; Okazaki, R.; Morokuma, K. *J. Am. Chem. Soc.* **1987**, *109*, 4142.

(51) Fueno, T.; Yokoyama, K.; Takana, S. *Theor. Chim. Acta* **1992**, *82*, 299.

(52) Takana, S.; Fueno, T. *Theor. Chim. Acta* **1994**, *87*, 431.

(53) Li, Y.; Iwata, S. *Bull. Chem. Soc. Jpn.* **1997**, *70*, 79.

(54) Nguyen, M. T.; Sumathi, R.; Sengupta, D.; Peeters, J. *Chem. Phys.* **1998**, *230*, 1.

(55) Dunning, T. H. *J. Chem. Phys.* **1989**, *90*, 1007.

(56) *MOLPRO* (http://www.tc.bham.ac.uk/molpro/). MOLPRO is a package of ab initio programs written by Werner, H.-J.; Knowles, P. J. with contributions from Almlof, J.; Amos, R. D.; Berning, A.; Cooper, D. L.; Deegan, M. J. O.; Dobbyn, A. J.; Eckert, F.; Elbert, S. T.; Hampel, C.; Lindh, R.; Lloyd, A. W.; Meyer, W.; Nicklass, A.; Peterson, K.; Pitzer, R.; Stone, A. J.; Taylor, P. R.; Mura, M. E.; Pulay, P.; Schutz, M.; Stoll, H.; Thorsteinsson, T.

(57) Werner, H.-J.; Knowles, P. J. *J. Chem. Phys.* **1985**, 82, 5053. Knowles, P. J.; Werner, H.-J. *Chem. Phys. Lett.* **1985**, 115, 259. Werner, H.-J.; Knowles, P. J. *J. Chem. Phys.* **1988**, 89, 5803. Knowles, P. J.; Werner, H.-J. *Chem. Phys. Lett.* **1988**, 145, 514.

(58) Herzberg, G. *Molecular Spectra and Molecular Structure III. Electronic Spectra and Electronic Structure of Polyatomic Molecules*; Van Nostrand: New York, 1966.

(59) *VARIFLEX-version 1.0* (http://chemistry.anl.gov/chem-dyn/VariFlex) VARIFLEX is a freeware program package for calculating gas-phase reaction rates written by Klippenstein, S. J.; Wagner, A. F.; Robertson, S. H.; Dunbar, R. C.; Wardlaw, D. M. in 1999.